HHS Public Access

Author manuscript

Cancer Res. Author manuscript; available in PMC 2022 March 15.

Published in final edited form as:

Cancer Res. 2021 September 15; 81(18): 4874–4885. doi:10.1158/0008-5472.CAN-20-3898.

Mapping mechanical properties of the tumor microenvironment by laser speckle rheological microscopy

Zeinab Hajjarian[1], **Elena F. Brachtel**[2,3], **Diane M. Tshikudi**[1], **Seemantini K. Nadkarni**[1,*]

[1]Wellman Center for Photomedicine, Massachusetts General Hospital, Harvard Medical School, 40 Blossom Street, BAR7, Boston, MA, 02114.

[2]Department of Pathology, Massachusetts General Hospital, Harvard Medical School, 55 Fruit St, Boston, MA, 02114.

[3]Department of Pathology, Maastricht University Medical Center, 25 P. Debyelaan, 6229 HX Maastricht, Netherlands.

Abstract

Altered mechanical properties of the tumor matrix have emerged as both the cause and consequence of breast carcinogenesis. Increased tumor stiffness has traditionally provided a viable metric to screen for malignancies via palpation or imaging. Previous studies have demonstrated that the micro-scale mechanical properties of the cell substrate influence tumor proliferation and invasive migration in vitro. Nevertheless, the association of the mechanical microenvironment with clinical hallmarks of aggressiveness in human breast tumors, including histopathological subtype, grade, receptor expression status, and lymph node involvement is poorly understood. This is largely due to the lack of tools for mapping tumor viscoelastic properties in clinical specimens with high spatial resolution over a large field-of-view (FoV). Here we introduce laser Speckle rHEologicAl micRoscopy (SHEAR) that for the first time enables mapping the magnitude viscoelastic or shear modulus, $|G^*(x,y,\omega)|$, over a range of frequencies (ω=1-250 rad/s) in excised tumors within minutes with a spatial resolution of ~50 μm, over multiple cm^2 FoV. Application of SHEAR in a cohort of 251 breast cancer specimens from 148 patients demonstrated that $|G^*(x,y,\omega)|$ ($\omega=2\pi$ rad/s) closely corresponds with histological features of the tumor, and that the spatial gradient of the shear modulus, $\|\nabla|G^*(x,y,\omega)\|$, is elevated at the tumor invasive front. Multivariate analyses established that the metrics, ($|G^*|$) and ($\|\nabla|G^*\|$), measured by SHEAR are associated with prognosis. These findings implicate the viscoelastic properties of the tumor microenvironment in breast cancer prognosis and likely pave the path for identifying new modifiable targets for treatment.

Significance: Laser speckle rheological microscopy establishes the links between microscale heterogeneities of viscoelasticity and histopathological subtype, tumor grade, receptor expression, as well as lymph node status in breast carcinoma.

[*]**Corresponding Author:** Seemantini K. Nadkarni, Ph.D., 40 Blossom Street, Bartlett Hall Room 720, Boston, MA 02114, snadkarni@mgh.harvard.edu, Phone: 617-724-1381, Fax:617-726-4103.

The authors have no conflict of interest.

Keywords

Breast cancer; tumor microenvironment; tumor heterogeneity; viscoelastic properties; stiffness; optical imaging

Introduction

It is increasingly recognized that the pathogenesis and progression of breast carcinoma are guided by the mechanical transformation of the tumor microenvironment (1-3). *In vitro* studies demonstrate that altered mechanical properties of the extra-cellular matrix (ECM) promote neoplastic transformation, differentiation, growth, and migration of mammary cells (2-4). Although these insights are well-established through *in vitro* mechanobiology studies, their implications for the clinical course of disease remain unclear (5-8). Breast carcinomas are miscellaneous, categorized by their histological and molecular subtypes, grade, and lymph node status (9,10). These prognostic criteria determine aggressiveness, predict response to therapy, and suggest modifiable targets for treatment (10). The relationships between mechanical remodeling of tumors and these prognostic criteria are poorly understood. If the link between micromechanical features and clinical phenotypes is identified, prognostic classification of breast malignancies may be improved. Moreover, novel therapies could be developed based on modifying the micro-mechanical drivers of carcinogenesis.

Increased stiffness or elasticity, a consequence of desmoplastic reaction, has been linked to metastasis and drug resistance in solid tumors (2,11-15). However, breast tissue is not merely elastic, but rather exhibits both viscous and elastic behaviors under different loading conditions, best characterized by the frequency-dependent complex viscoelastic modulus also termed the shear modulus, $G^*(\omega)$ (16). Emerging evidence suggests that tumor cells sense both the microscale elastic and viscous traits of their substrate and respond to viscous dissipation by either activating or suppressing the oncogenic reprogramming, in ways not explained by changes in elasticity alone (16,17). Moreover, spatial heterogeneities of $|G^*(\omega)|$ within the tumor may create gradients, i.e. $\|\nabla|G^*(\omega)|\|$, that foster directional migration and invasion (7).

Histopathological analyses reveal that breast cancer subtypes exhibit distinct tumor and stromal composition and architecture (9,10). Deposition and rearrangement of the ECM components by neoplastic and host cells in turn cause mechanical heterogeneities, lending credence to the premise that the tumor mechanical microenvironment is associated with the histological subtypes (1). Mechanical properties of the ECM may regulate mitotic activity and subsequently govern histological grade (11,14,18). Expression of estrogen, progesterone, and human epidermal growth factor2 (ER/PR/HER2) receptors in tumor cells are associated with fibroblast and immune cell infiltration. The subsequent fibrotic and inflammatory responses in turn alter the mechanical microenvironment of the tumor and may link viscoelastic properties to molecular expressions (1,19-21). Given that preferential invasion of tumor cells is orchestrated by perpendicularly aligned ECM fibers at the tumor-ECM interface, also termed the invasive front (IF), mechanical heterogeneities are expected

to correlate with lymph node involvement (7,22,23). Despite growing evidence, the links between tumor viscoelasticity and these prognostic criteria are missing and the potential implications for diagnosis and treatment remain distant, largely due to absence of tools for mapping the $|G^*(\omega)|$ with high resolution.

Here, we introduce laser Speckle rHEologicAl micRoscopy (SHEAR) that estimates and maps the shear modulus, $G^*(x,y,\omega)$, of tumors with high spatial resolution over large field-of-views (FoVs). SHEAR is developed by modifying an inexpensive upright microscope to illuminate the specimen and capture time series of speckle patterns, formed by multiple scattering and interference of coherent light from tissue particles (Fig. 1(A, B)). Thermal motion of intrinsic light-scattering particles within tissue creates dynamic phase shifts and speckle intensity modulations at a rate commensurate with the extent of particle displacements and in turn the viscoelastic properties of tissue microenvironment (Fig. 1(C-E)). Consequently, in breast, softer adipose and glandular tissues exhibit rapid speckle intensity fluctuations compared to the fibrous ECM. Therefore, by measuring the mean square displacement, MSD, of scattering particles from temporal speckle intensity fluctuations, and estimating the radius of scattering particles, the frequency-dependent complex shear modulus, $G^*(\omega)$, can be assessed over a range of angular frequencies, ω. SHEAR is similar to dynamic light scattering (DLS) in that it measures the $G^*(\omega)$ from the thermal fluctuations of scattering particles (24). However, unlike DLS, SHEAR is not limited to single scattering events in transparent samples and instead exploits multiple scattering from an ensemble of intrinsic light scatterers to measure heterogenous, stiffer turbid samples including tissue.

We demonstrate that SHEAR can rapidly map the magnitude of the complex shear modulus, $|G^*(x,y,\omega)|$ with 50 μm spatial resolution over scalable FoVs of multiple cm^2, covering tumor epithelium, invasive front (IF), and peri-tumoral ECM within minutes. The $|G^*(x,y,\omega)|$ maps plotted at a frequency of $\omega=2\pi$ rad/s, closely correspond with histo-morphological features, with elevated gradient of shear modulus, $\|\nabla|G^*(x,y,\omega)\|$, observed at the IF. Our study shows for the first time that shear modulus and the indices of mechanical heterogeneity estimated by SHEAR are associated with prognostic indicators of histological subtype, receptors' expression status, grade, and lymph node involvement. These results establish the utility of SHEAR technology for studying the viscoelastic behavior of breast cancer and likely open impactful avenues for integrating these new micromechanical metrics in the diagnosis, treatment planning, and development of novel therapeutics.

Materials and Methods

SHEAR Setup

A schematic of the SHEAR optical instrument is displayed in Fig. 1(A). A laser beam (633 nm, Helium-Neon, 45 mW, JDSU) was focused at the back focal plane of the objective (10x Olympus, NA=0.25), creating a 1.6 mm diameter beam (5 mW) at the sample surface. Back-scattered time-varying speckle patterns (Fig. 1(B)) were imaged via the objective and tube lens (f=175 cm) by a CMOS camera (Basler, ACa 2000-340 km, Germany) operated at 250 frames per seconds (fps). The sample was placed on a motorized stage interfaced with a step-motor controller (ESP 301-3G, Newport Corporation, USA). Speckle frame series

were acquired over a region of interest (RoI) of 500×500 μm and the sample was translated in 450 μm steps in a serpentine pattern, maintaining a 10% of overlap between acquired RoIs to scan the entire sample. For each RoI, speckle frames were acquired for 1 second at 250 fps. Brightfield images were acquired simultaneously to facilitate co-registration with histopathology. A Custom-built C++ software was used for instrument automation to synchronize the motion controller and camera trigger.

SHEAR image reconstruction

Methods detailed in our prior studies were extended to estimate the frequency-dependent shear modulus, G*(x,y,ω), at each pixel location, (x,y), from time-varying speckle frames (25-30). The speckle intensity autocorrelation, $g_2(x,y,t)$, was measured from the speckle time series and the MSD of local scattering particles was subsequently calculated (Supplementary Method 1, Fig. S1(A-B)). The G*(x,y,ω) was determined by substituting the MSD in the generalized Stokes-Einstein relation (GSER) via $G^*(x,y,\omega)=\frac{K_BT}{\pi a i\omega \mathcal{F}\{\langle \Delta r^2(x,y,t)\rangle\}}$ where, $\mathcal{F}$ is Fourier transform and *a* is the scattering particle radius (Supplementary Methods 1, Fig. S1(C)) (25-29,31,32). The particle radius, *a,* was estimated by calculating the ratio of the decay rates of $g_2(t)$ curves acquired at perpendicular and parallel polarizations (Supplementary Method 2, Fig. S2 (A-D)). The magnitude of the shear modulus, |G*(x,y,ω)|, was evaluated over a frequency range, 1<ω<250 rad/s, determined by the acquisition time (1s) and the camera frame rate (250 fps). Although |G*(x,y,ω)| was calculated over the entire range, 1<ω<250 rad/s, for ease of comparison with histopathology and correspondence with rheometry, in this paper we display |G*(x,y)| maps at a single frequency ω=2π rad/s (f=1 Hz). From the |G*(x,y)| maps, the following metrics were calculated: the spatially-averaged $\overline{|G^*|}$ over all pixels (x,y); the shear modulus gradient, ‖∇|G*(x,y)|‖; the spatially-averaged gradient, $\overline{|\nabla|G^*||}$; heterogeneities in $\overline{|G^*|}$ in the tumor epithelium vs stroma; and the information entropy, H, of the |G*(x,y)| maps (Supplementary Method 4, Fig. S3). Rewriting the shear modulus as G*(ω)=G'(ω)+iG''(ω), further permitted extracting the elastic, G'(ω), and viscous, G''(ω), moduli as the real and imaginary components (Supplementary Method 1). Fig. 1(D) displays representative $g_2(t)$ and MSD (inset) for a normal fibroadipose breast tissue. The frequency-dependent $\overline{|G^*(\omega)|}$, $\overline{G'(\omega)}$, and $\overline{G''(\omega)}$ obtained by SHEAR are shown in Fig. 1(E): all three curves closely agree with the results of conventional rheometry at frequencies below ω=20π (62.8) rad/s, (i.e. 10 Hz), above which the accuracy of rheometer measurements is influenced by the inertial effects as discussed below.

Study design

The study was approved by the institutional review board of Massachusetts General Hospital (MGH IRB#2011P000301). Fresh, excess, and de-identified human breast specimens (N=251) were collected from 126 patients undergoing breast cancer surgery (mastectomy or lumpectomy, 1 male, 125 females) and 22 patients undergoing breast reduction surgery, between March 2015 and October 2019. The clinical diagnosis for each specimen, the tumor size, histopathological grade, hormonal receptor status, lymph node status, and history of neoadjuvant chemotherapy or radiation therapy was obtained from pathology records. Table

1 summarizes the tumor diagnoses. The samples were refrigerated at 4° C and imaged within two hours of being grossed. Prior to imaging, the sample was marked with ink, warmed to 37° C in a water bath, and loaded onto the motorized linear stage within the SHEAR device (Fig. 1(A)). After imaging, each sample was fixed in 10% formalin, sectioned at 100 μm increments in depth (7 μm thick sections), and stained with hematoxylin and eosin (H&E), and Picrosirius Red (PSR). The H&E slides were digitized using Nano-zoomer whole slide scanner (2.0 HT, Hamamatsu, Japan). PSR slides were digitized using a circularly-polarized light microscope (BX43, Nikon, USA, 4x). Fiducial ink marks in the sample photographs and brightfield images were used to co-register the SHEAR data with histology. Pathologist (EFB) blinded to the SHEAR data provided histopathological analysis from H&E slides.

Mechanical rheometry

A conventional strain-controlled rheometer (ARG2, TA instruments Inc., USA) was used to evaluate |G*(ω)| for a subset of N=28 breast tissue specimens (Supplementary Method 5). The sample was sandwiched between the rheometer plates (8mm diameter) and a frequency sweep was performed over ω = 0.628-250 rad/s, while maintaining the strain below 0.5%, to obtain G*(ω).

Statistical analysis

Linear regression analysis investigated the correlations between SHEAR measurements, collagen content and rheometer measurements. Two-way analysis of variance (ANOVA) was used to evaluate associations between prognostic criteria and SHEAR measurements (Prism, GraphPad Inc., USA). Pairwise comparisons were performed using Tukey's method (for multiple comparisons), un-paired (between independent groups) or paired t-tests (between dependent groups). Multivariate analysis and a generalized estimating equation (GEE) model were used to identify prognostic criteria that significantly and independently correlated with $\overline{|G^*|}$ and $\overline{|\nabla|G^*||}$ (SPSS, IBM Crop., USA). In all cases, $p<0.05$ was considered statistically significant.

Results

SHEAR |G*(x,y)| maps correspond with breast histopathology.

Figure 2(A) shows the |G*(x,y)| map of a normal breast specimen. Within adipose regions (H&E image, Fig. 2(B)), low |G*(x,y)| values ~0.05-3 kPa were observed (white arrows), whereas in fibrous tissue |G*(x,y)| increased to 5-20 kPa, consistent with the bright pink hues in H&E image and the collagen fiber network in PSR slide (Fig. 2(C)) (magenta arrows). In glandular tissue, including ducts and terminal duct-lobular units (TDLU), |G*(x,y)| was ~3-5 kPa (yellow and red arrows), with higher moduli observed near ducts than around TDLU, consistent with the expected stiffness variations in the vicinity of glandular tissues (22). Linear regression analysis indicated a significant positive correlation between the spatially-averaged $\log(\overline{|G^*|})$ obtained by SHEAR and collagen content, measured as the percentage area occupied by orange-yellow hues of circularly-polarized light microscopy images of PSR-stained sections (N=251, r=0.69, p<0.0001) (Fig. 2(D)). The y-axis represented the $\log(\overline{|G^*|})$, because while collagen density saturates at 100%,

fiber alignment and cross-linking could substantially increase $\overline{|G^*|}$ even for small changes in total collagen.

Frequency-dependent SHEAR measurements correlate with standard rheometry.

In Fig, 2 (E-G), the spatially-averaged modulus, $\overline{|G^*(\omega)|}$ measured by SHEAR is compared with that measured by a mechanical rheometer in 28 breast tumors at three distinct frequencies. At low frequencies, $\overline{|G^*(\omega)|}$ measured by SHEAR exhibits a strong correlation with corresponding rheometer measurements (at $\omega=\pi$ rad/s: R=0.78, $p<0.0001$; and $\omega=2\pi$ rad/s: R=0.76, $p<0.0001$) over a large range of moduli values (0.7 – 17kPa). We further observe a good correlation with rheometer measurements, which is maintained up to $\omega=10\pi$ rad/s (5Hz, R=0.64, $p = 0.0002$). At $\omega=20\pi$ rad/s the correlation drops to R=0.41 ($p=0.04$) likely due to inertial effects of the rheometer at higher frequencies (Supplementary Method 5).

SHEAR maps are influenced by histopathological subtypes of breast cancer.

$\overline{|G^*|}$ is excessively elevated in aggressive IMPC compared to other subtypes: Figures 3 (A), (E), (I), and (M) present the $|G^*(x,y)|$ maps of typical IMC, IDC, IPC, and IMPC tumors, the corresponding $|\nabla|G^*(x,y)||$ (Figs. 3 (B), (F), (J), and (N)), H&E images (Figs. 3 (C), (G), (K), and (O)), and PSR sections (Figs. 3 (D), (H), (L), and (P)). In IMC (Fig. 3(A)), regions that exhibit $|G^*(x,y)|$~0.2-3 kPa coincide with the mucinous compartments in the H&E image. These compliant areas contrast the regions of increased $|G^*(x,y)|$ ~30 kPa, corresponding to collagen-rich stroma in the PSR image. In the $|G^*(x,y)|$ map of Fig. 3(E), which represents an IDC tumor with a ductal carcinoma in-situ (DCIS) component, the tumor epithelium exhibits low values of $|G^*(x,y)|$ ~0.1-5 kPa in regions where tumor cells are confined within ducts (DCIS, yellow arrows) and when tumor cells breach out as invasive carcinoma (red arrows). Moreover, the necrotic cores of DCIS exhibits a lower $|G^*(x,y)|$ ~ 3 kPa. Unlike epithelial regions, $|G^*(x,y)|$ exceeds 5 kPa within the stroma: around DCIS, $|G^*(x,y)|$ is ~10 kPa, whereas for desmoplastic stroma of the IDC component, $|G^*(x,y)|$ ~10-20 kPa. The moderately aggressive IPC subtype in Fig. 3(I) exhibits distinct features with very low $|G^*(x,y)|$ ~0.1-1 kPa corresponding to the highly vascularized epithelium, comprising low viscosity blood, and a central stromal stem of slightly increased $|G^*(x,y)|$ ~5 kPa. Fig. 3(M) displays the $|G^*(x,y)|$ map of IMPC, which is associated with a particularly high rate of metastasis and poor prognosis. The reduced $|G^*(x,y)|$ ~3kPa areas correspond to highly malignant cells in the H&E image with thin spikes of increased $|G^*(x,y)|$ that extend from the stroma and closely correspond to collagen architecture in the PSR section. These bundled and stiffened collagen fibers, aligned perpendicular to IF, are believed to support the preferential migration and invasion of tumor cells (12). A highly contrasting $|G^*(x,y)|$ ~30 kPa in Fig. 3(M) coincides with the accumulation, thickening, and occasional perpendicular realignments of collagen fibers in the PSR image of Fig 3(P). Consistent with $|G^*(x,y)|$ maps of Fig. 3, ANOVA of 251 human breast specimens from 148 patients in our cohort reveals that $\overline{|G^*|}$ is significantly different among benign and tumor specimens of distinct histological subtype ($p < 0.0001$) (Fig. 3(Q)). Tukey's multiple comparisons indicates that adipose tissue exhibits a significantly lower $\overline{|G^*|}$ than benign fibrous, IDC, ILC, and IMPC. In addition, $\overline{|G^*|}$ in both fibrous

tissues and IPC is significantly lower than IMPC, given the prominently desmoplastic stroma of the latter. Multivariate analysis indicates that histological subtype is significantly associated with $\overline{|G^*|}$ ($p<.004$) with aggressive IMPC tumors exhibiting highly elevated $\overline{|G^*|}$ (Supplementary Tables S1 & S2).

The |∇|G*(x,y)|| is significantly increased in aggressive subtypes: The IF interface between the epithelium and stroma are delineated by an abrupt increase in $|G^*(x,y)|$ and intensified $|\nabla|G^*(x,y)||$ for all tumors in Fig. 3. Among all lesions, the $|\nabla|G^*(x,y)||$ of IMPC in Fig. 3(N) exhibits the highest value at the IF (white arrow). ANOVA performed in 38 out of 111 tumor specimens that present a clear IF based on the H&E, suggests that the $\overline{|\nabla|G^*||}$ at IF is significantly different among subtypes, being highest in IMPC and lowest in IPC (Fig. 3(R)). Subsequently, multivariate analysis confirms that histological subtype is the most influential prognostic criteria independently associated with $\overline{|\nabla|G^*||}$ ($P<0.0001$) (Supplementary Tables S3 & S4).

|G*(x,y)| maps of breast carcinoma are influenced by tumor grade.

$\overline{|G^*|}$ is reduced in high-grade tumors: Figures 4 (A), (E) and (I), show $|G^*(x,y)|$ maps of tumors with increasing grades, the corresponding $|\nabla|G^*(x,y)||$ (Figs. 4 (B), (F), and (J)), H&E images (Figs. 4 (C), (G), and (K)), and PSR sections (Figs. 4(D), (H), and (L)). The $|G^*(x,y)|$ within the tumor epithelium reduces with grade from ~6.5 kPa in grade I (Fig. 4(A)), to ~4.8 kPa in grade 2 (Fig. 4(E)), and ~2 kPa in grade 3 (Fig. 4(I)) tumors. By contrast, the $|G^*(x,y)|$ of the tumor stroma, in grade 1 and 2 tumors with perceptible stromal components, is considerably elevated to 30 kPa as seen in the left half of Fig. 4(A) and lower half of Fig. 4(E), consistent with densely packed collagen fibers seen in PSR sections of Fig. 4(D) and 4(H). In the grade 2 tumor of Fig. 4(E), sporadic bands of increased $|G^*(x,y)|$ of up to 7 kPa in the compliant regions correspond to sparse intra-tumoral ECM fibers in the epithelium, as evidenced by the H&E image (Fig.4(G)). Unlike Figs. 4(A) and 4(E), the $|G^*(x,y)|$ map of the grade 3 lesion in Fig. 4(l) is mostly complaint and the H&E image (Fig. 4(K)) reveals a highly cellular tumor. Moreover, the extremely reduced $|G^*(x,y)| < 2$ kPa in Fig. 4(I) correspond to mitotic cells. These contrast the neighboring areas of $|G^*(x,y)|$ ~5 kPa (red arrows) that coincide with necrosed cells (yellow arrows) in Fig. 4(K). From Fig. 4, it appears that the amount of peripheral stroma, and in turn the overall $\overline{|G^*|}$ is reduced in high-grade lesions. ANOVA consequently confirms that $\overline{|G^*|}$ reduces with tumor grade, and grade 3 lesions exhibit the lowest $\overline{|G^*|}$ values (Fig. 4(M)) ($p<0.05$). Multivariate analysis subsequently indicates that tumor grade is significantly associated with $\overline{|G^*|}$ ($P< 0.002$), (Supplementary Tables S1&S2).

High-grade tumors exhibit increased $\overline{|\nabla|G^*||}$ at the invasive front: Strong mechanical contrast between the tumor epithelium and stroma leads to an increased $\overline{|\nabla|G^*||}$ at the IF, as evidenced by Figs. 4(B) and 4(F). In contrast, grade 3 tumor depicted in Fig. 4(I) is more necrotic than fibrotic and lacks a perceptible IF. Nevertheless, a subset of grade 3 lesions in our cohort, e.g. Fig. 3(M), exhibit considerable peri-tumoral fibrosis and an intensified $\overline{|\nabla|G^*||}$ at the IF. ANOVA results show that $\overline{|\nabla|G^*||}$ is

significantly different among tumors of different grades, with grade 3 lesions exhibiting larger gradients than grade 2 tumors at the IF (Fig. 4(N)). However, when considered collectively with other prognostic criteria in a multivariate analysis, tumor grade is not independently associated with $\overline{|\nabla|G^*||}$.

$\overline{|G^*|}$ is significantly lower in the tumor epithelium versus stroma: To investigate heterogenous moduli distributions, |G*(x,y)| maps were separated into epithelium and stroma components (Fig. 5(A), (E), and (G)), through multiplication with spatial masks (Fig. 5(D), Supplementary Method 4). This analysis was performed in 58 (of 111) tumors in which both components could be clearly seen in H&E images (Fig. 5(B), (F), and (H)). Figure 5 (A), (E), and (G) show distinct variations in |G*(x,y)| distributed within epithelium and stroma of a grade 1, IDC tumor: significantly lower moduli (~10kPa) are observed within the epithelium versus the stroma (~20-30kPa).

The corresponding |∇|G*(x,y)|| is considerably elevated at the epithelium-stroma interface (Fig. 5(C)). The pooled data (Figs. 5 (I, J)) of $\overline{|G^*|}$ indicate that both epithelial and stromal moduli significantly reduce with the tumor grade (p=0.0001). Paired t-tests further shows that within each grade, stroma is significantly stiffer than epithelium. Moreover, grade 1 tumors entail both a stiffer stroma and epithelium than grade 3 lesions, suggesting that malignant, high-grade cells are progressively more compliant (33).

Intra-tumoral heterogeneities of |G*(x,y)| maps were also estimated by calculating the information Entropy (Supplementary Methods 4). Entropy was measured in 106 (of 111) tumors for which the |G*(x,y)| maps were free of mosaicking artifacts. We observe that Entropy trends towards lower values with increasing tumor grade (Fig. 5(K)), supporting our above findings that the |G*(x,y)| in high grade cellular masses is uniformly low.

Mechanical characteristics of tumor micro-environment are driven by receptor expressions.

Molecular expressions are linked to elevated $\overline{|G^*|}$: Figures 6 (A), (E), and (I) show |G*(x,y)| maps of grade 3 tumors with different molecular expressions, the corresponding |∇|G*(x,y)|| (Figs. 6 (B), (F), and (J)), H&E images (Figs. 6 (C), (G), and (K)), (Figs. 6(D), (H), and (L)). Epithelial areas exhibit lower |G*(x,y)| (~0.1-5kPa), where tumor cells mingle with adipose tissue, degenerated ECM fibers, and immune infiltrates. In contrast, the stroma exhibits distinctively higher |G*(x,y)| values. In the ER/PR+, HER2− tumor, |G*(x,y)| increases up to 20 kPa (Fig. 6(A)), corresponding with bright red collagen bundles (Fig. 6(D)) within the fibrotic stroma. In ER/PR+, HER2+ tumor, |G*(x,y)| features islands of moderately increased |G*(x,y)| up to 10 kPa, harboring spots of elevated |G*(x,y)|~30 kPa (Fig. 6(E)) that correspond with thick collagen fibers and micro-calcifications in H&E. Finally, the ER/PR−, HER2− (triple negative breast cancer, TNBC) lacks a significant fibrotic component (Figs. 6 (K,L)) and presents moderate values of |G*(x,y)| around necrosed areas. From these |G*(x,y)| maps it appears that TNBC tumors exhibits a significantly reduced $\overline{|G^*|}$ compared to ER/PR+, likely due to higher cell proliferation and more necrosis than fibrosis in this aggressive subtype (34). Subsequently, unpaired

t-tests indicates that $\overline{|G^*|}$ is significantly higher in ER+ and PR+ lesions (Fig. 6 (M-N)). Multivariate analysis, however, shows that only the PR status significantly affects $\overline{|G^*|}$ (p=.043, Supplementary Tables S1 & S2). No significant association is identified in $\overline{|G^*|}$ with respect to HER-2 status (Fig. 6(O)).

$\overline{\nabla|G^*|}$ is increased at the invasive front of tumors expressing ER, PR, and HER2 receptors: The $|\nabla|G^*(x,y)|\|$ is elevated at the IF of the ER+/PR+/HER2− lesion (Fig. 6(B)), whereas regions of elevated $|\nabla|G^*(x,y)|\|$ are observed in the vicinity of microcalcifications for the ER+/PR+/HER2+ tumor (Fig. 6(E)). In the TNBC tumor (Fig. 6(I)), $|\nabla|G^*(x,y)|\|$ is mildly elevated around necrotic regions. Subsequently, un-paired t-test shows that $\overline{|\nabla|G^*||}$ is significantly higher in ER+ and PR+ tumors (Fig. 6 (P, Q)). For these tumors, a higher $\overline{|G^*|}$ is noticed as well, likely dominated by the stromal components, which in turn give rise to higher $\overline{|\nabla|G^*||}$ at the IF. The $\overline{|\nabla|G^*||}$ also trends higher in HER2+ lesions, although this is not significant (Fig. 6 (R)). Multivariate analysis indicates that only ER status (P=0.023) independently affects $\overline{|\nabla|G^*||}$ (Supplementary Tables S3 & S4).

Micromechanical characteristics of tumors with lymph node involvement.

SHEAR maps displayed in Figs. 3(A), 3(M), 4(E), 5(A), and 6(A) are from tumors with lymph node involvement (LN+). Although majority of LN+ specimens exhibit a trend towards increased $|G^*(x,y)|$ in tumor periphery, multivariate analysis does not find a significant association in $\overline{|G^*|}$ with respect to LN status (Supplementary Fig. S4 (A)). In contrast, $\overline{|\nabla|G^*||}$ is significantly higher in LN+ specimens ($p<0.0001$, Supplementary Fig. 4S (B)). Multivariate analysis show that LN status (P=0.047) is independently associated with $\overline{|\nabla|G^*||}$ (Supplementary Tables S3 & S4). These findings agree with previous hypotheses on directional invasion of cancer cells, suggesting that the metastatic migration is derived by the $\overline{|\nabla|G^*||}$, rather than overall tumor $\overline{|G^*|}$ (35,36).

Discussion

Breast carcinoma are frequently classified based on histological subtype, grade, molecular receptors' expression, and lymph node involvement. These prognostic criteria likely both influence and are influenced by the viscoelastic modulus, $|G^*(x,y,\omega)|$ of the tumor microenvironment (1-3,7,12,21,22,37). In clinical settings, ultrasound and magnetic resonance elastography (USE, MRE) have been shown to detect the increased elasticity of tumor tissue (38-42). Nevertheless, due to low resolution, these bulk-scale measurements remain insufficient for assessing nuanced associations of tumor histopathology with stiffness. Recently, atomic force microscopy (AFM) enabled high-resolution, albeit laborious, mapping of sub-surface elastic properties across small FoVs (~10s of μm), over hours, in frozen sections and demonstrated the link between micro-mechanical heterogeneities and invasive subtypes (36,43). Moreover, optical coherence elastography (OCE) enabled tumor margin delineation based on micro-scale deformations of breast tissue over FoVs of multiple cm^2 (44,45). However, both techniques contact the tissue to apply

a static load and require apriori knowledge of stress to evaluate the strain response, and thus only indirectly assess the static elastic properties, but fail to recapitulate the dynamic viscoelastic behavior of tumors (36,43-45).

Here, we have demonstrated for the first time the capability of SHEAR to estimate and map the frequency-dependent viscoelastic modulus, $|G^*(\omega)|$, with microns-scale resolution, over centimeters of FoVs in excised human breast specimens, in a non-contact manner. SHEAR captures multiply-scattered, multi-speckle patterns; therefore, speckle intensity fluctuations are sensitive to even 10's of nm displacements of individual scattering particles. This in turn permits probing $|G^*(\omega)|$ over a wide range of highly complaint to very stiff breast tissue specimens (Fig. 1, Supplementary Fig. S1). Using homogenous hydrogel materials, we have previously demonstrated that $|G^*(\omega)|$ values measured from speckle intensity fluctuations were closely correlated with both rheometer and AFM measurements and spanned a large moduli range of 0.1-40 kPa (29). We have extended these prior studies to demonstrate the strong correlation between $|G^*(\omega)|$ measured by SHEAR and mechanical rheometry in the breast tissue specimens at multiple frequencies (Fig. 2(E-G)). The larger spread of data points, compared to our prior studies in homogenous hydrogels, is likely due to challenges associated with conducting rheometry in tissue, differences between the length scales of rheometer and SHEAR measurements, and tissue heterogeneity (Supplementary Method 5). The range of moduli measured in our study are comparable to those previously measured by MRE in typical benign and malignant breast tissue (42); however, SHEAR measurements were significantly larger than previous AFM results. This was in part due to the smaller length scale and FoV, and superficial probing depth of AFM that likely weighted the measured elastic moduli towards lower values in these prior studies.

To estimate $|G^*(\omega)|$ via GSER, the sphere-equivalent particle radius, a, was estimated by comparing $g_2(t)$ at perpendicular and parallel polarization states, $g_{2\perp}(t)$ and $g_{2\parallel}(t)$, respectively (Supplementary Method 2). A limitation of our study is that a single value of a=100 nm was used for all 251 specimens based on the above methods. However, scattering particles' radius, a, could vary both among different tissue types and within different regions of tissue. For example, in a representative set of 23 breast tissues, we estimated that a varied by up to ±35 nm, suggesting a maximum variability of 35% in the estimated $|G^*(\omega)|$ values, which likely contributed in part to the spread of $|G^*(\omega)|$ in the scatter plots of Fig. 2(E-G). In future, this variability may be significantly reduced by calculating spatially-varying ratios of $g_{2\perp}(t)$ and $g_{2\parallel}(t)$ and estimating distinct particle radii while scanning the sample.

In addition to scattering particle size, biological tissue present a variety of length scales, with the ECM mesh structure varying over a large range of pore sizes from tens of nm to a few microns (46). Therefore, depending on the relative size of scattering particles, a, and pore size, δ, the MSDs of scattering particles probe distinct mechanical behaviors of the tissue constituents (47). More specifically, in weaker, unlinked ECM regions, where $a<\zeta$, the motion of scattering particles is largely diffusive and the MSD reflects the local viscoelasticity of the cellular, necrotic or lipid components depleted of ECM linkages. On the other hand, in dense ECM network, where $\xi<a$, the scattering particles are effectively coupled to the matrix and the MSD probes the viscoelastic properties of the cross-linked ECM network. This in fact is precisely the source of high mechanical

contrast in SHEAR measurements. In other words, in the context of heterogeneous tissue, pixel-by-pixel analysis of multi-speckle frames in SHEAR enables probing local scattering particles whether they are restricted in small pores of dense and desmoplastic ECM, or diffuse between the looser, un-crosslinked meshwork. Thus, replacing the MSD and *a* in the GSER yields the local viscoelastic properties, at scales larger than the size of scattering particles, yet small and inaccessible to macroscopic rheometry (47,48). This could likely further explain the spread in the scatter plots of Fig. 3(E-G).

The frequency range of $|G^*(\omega)|$ is mainly governed by the acquisition duration and frame rate (Supplementary Method 1). The Basler acA2000-340km camera permitted a frequency limit of 6000 rad/s; however, in our study we limited the frame rate to 250 fps with the goal of comparing SHEAR results with mechanical rheometry, which is limited by tool inertia at higher frequencies.

While this study is limited to the investigation of the shear modulus, $|G^*(\omega)|$, additional information may be gained by extracting the relative contributions of $G'(\omega)$ and $G''(\omega)$. In an ongoing pilot study, we observed that in highly desmoplastic tumors, with restricted particle displacements, G' dominates the G*, whereas for highly cellular, vascular, or mucinous lesions, with diffusive particle displacement, G'' is likely the prominent contributor. While representative curves are presented in this paper (Fig. 1 and Supplementary Fig. 1S) to demonstrate the opportunity to estimate $G'(\omega)$ and $G''(\omega)$, a comprehensive investigation is yet necessary to fully investigate the complex associations between distinct elastic and viscous moduli with tumor prognostic criteria. Similarly, for ease of interpretation with histopathology, shear moduli maps at a single frequency $\omega = 2\pi$ rad/s are presented. Yet, SHEAR may offer a wealth of information to investigate whether the frequency-dependent evolution of $|G^*(x,y,\omega)|$ presents additional, unique micro-mechanical markers for clinical prognostication.

Our results further confirmed the significant differences in average $\overline{|G^*|}$ among tumors of different prognostic criteria. The overall $\overline{|G^*|}$ was higher in aggressive histological subtypes, and in tumors enriched in hormonal and HER2 receptors, but reduced with histological grade, and remained indifferent with respect to lymph node status. The increased $\overline{|G^*|}$ in ER+ specimen agreed with previous accounts on enriched ER expression in mammographically dense patients (49). In addition, the reduced $\overline{|G^*|}$ in TNBC lesions was corroborated by prior ultrasound elastography studies and attributed to the elevated necrosis and diminished desmoplastic reaction in these lesions (50).

The distinct differences in $|G^*(x,y)|$ within the tumor epithelium and stroma components provided a unique perspective on the intra-tumoral heterogeneity. Intriguingly, certain micromechanical features were observed in aggressive tumors. For instance, the tumor epithelium in higher grade lesions was highly compliant, a finding that is corroborated by previous studies that suggest acute deformability of extremely malignant tumor cells (8,33). Furthermore, our finding that tumor stroma is significantly stiffer vs epithelium across all grades is supported by the well-established concept of the desmoplastic reaction (2). In addition, the reduction of entropy with grade likely suggests that in high-grade masses,

compliant, highly proliferative cells yield a mechanically uniform landscape. Increased $\overline{|\nabla|G^*||}$ at the IF of ER+, PR+, HER2+, and LN+ lesions was observed in our study. The role of stiffness gradients in directing local invasion has been demonstrated *in vitro* by using engineered gels of tunable elasticities and tracking the migratory behavior of seeded cells (6). Through characterizing the $\overline{|\nabla|G^*||}$ in clinical specimens, SHEAR may facilitate the translation of these fundamental mechanobiology concepts towards clinical diagnosis. By evaluating and identifying the micro-mechanical features shared between aggressive subgroups, SHEAR likely provides a unified understanding of the invasive pathophysiology beyond traditional phenotyping criteria (51).

Supplementary Material

Refer to Web version on PubMed Central for supplementary material.

Acknowledgments:

This work was supported in part by the NIH (NHLBI 5R01HL119867, PI: S. K. Nadkarni), American Society for Laser Medicine and Surgery research grant (PI: Z. Hajjarian), and Eleanore and Miles Shore Foundation Fellowship (PI: Z. Hajjarian). We would like to thank Arriane Garret for technical assistance. We sincerely thank Mohmmad Miri, Maxwell Hogue, Marina Kem, Rea Ruiz, Carolyn Mc Donagh, Haley Martin, and Tim Casson from MGH tissue repository for providing the human breast tissue specimens. We also thank Dr. Hang Lee of the Harvard Catalyst Program for providing statistical consultation on data analysis.

Financial Support:

This work was supported in part by the NIH (NHLBI 5R01HL119867, PI: S. K. Nadkarni), American Society for Laser Medicine and Surgery research grant (PI: Z. Hajjarian), and Eleanore and Miles Shore Foundation Fellowship (PI: Z. Hajjarian).

References:

1. Kaushik S, Pickup MW, Weaver VM. From transformation to metastasis: deconstructing the extracellular matrix in breast cancer. Cancer Metastasis Rev 2016;35:655–67 [PubMed: 27914000]
2. Paszek MJ, Zahir N, Johnson KR, Lakins JN, Rozenberg GI, Gefen A, et al. Tensional homeostasis and the malignant phenotype. Cancer cell 2005;8:241–54 [PubMed: 16169468]
3. Pickup MW, Mouw JK, Weaver VM. The extracellular matrix modulates the hallmarks of cancer. EMBO reports 2014;15:1243–53 [PubMed: 25381661]
4. Levental KR, Yu H, Kass L, Lakins JN, Egeblad M, Erler JT, et al. Matrix crosslinking forces tumor progression by enhancing integrin signaling. Cell 2009;139:891–906 [PubMed: 19931152]
5. Katira P, Bonnecaze RT, Zaman MH. Modeling the mechanics of cancer: effect of changes in cellular and extra-cellular mechanical properties. Front Oncol 2013;3:145 [PubMed: 23781492]
6. DuChez BJ, Doyle AD, Dimitriadis EK, Yamada KM. Durotaxis by Human Cancer Cells. Biophysical journal 2019;116:670–83 [PubMed: 30709621]
7. Oudin MJ, Weaver VM. Physical and Chemical Gradients in the Tumor Microenvironment Regulate Tumor Cell Invasion, Migration, and Metastasis. Cold Spring Harb Symp Quant Biol 2016;81:189–205 [PubMed: 28424337]
8. Spill F, Reynolds DS, Kamm RD, Zaman MH. Impact of the physical microenvironment on tumor progression and metastasis. Curr Opin Biotechnol 2016;40:41–8 [PubMed: 26938687]
9. Rakha EA, El-Sayed ME, Lee AH, Elston CW, Grainge MJ, Hodi Z, et al. Prognostic significance of Nottingham histologic grade in invasive breast carcinoma. Journal of clinical oncology : official journal of the American Society of Clinical Oncology 2008;26:3153–8 [PubMed: 18490649]
10. Weigelt B, Geyer FC, Reis-Filho JS. Histological types of breast cancer: how special are they? Mol Oncol 2010;4:192–208 [PubMed: 20452298]

11. Walker RA. The complexities of breast cancer desmoplasia. Breast Cancer Res 2001;3:143–5 [PubMed: 11305947]
12. Conklin MW, Keely PJ. Why the stroma matters in breast cancer: insights into breast cancer patient outcomes through the examination of stromal biomarkers. Cell adhesion & migration 2012;6:249–60 [PubMed: 22568982]
13. Netti PA, Berk DA, Swartz MA, Grodzinsky AJ, Jain RK. Role of extracellular matrix assembly in interstitial transport in solid tumors. Cancer Res 2000;60:2497–503 [PubMed: 10811131]
14. Shao ZM, Nguyen M, Barsky SH. Human breast carcinoma desmoplasia is PDGF initiated. Oncogene 2000;19:4337–45 [PubMed: 10980609]
15. Cox TR, Bird D, Baker AM, Barker HE, Ho MW, Lang G, et al. LOX-mediated collagen crosslinking is responsible for fibrosis-enhanced metastasis. Cancer Res 2013;73:1721–32 [PubMed: 23345161]
16. Chaudhuri O, Cooper-White J, Janmey PA, Mooney DJ, Shenoy VB. Effects of extracellular matrix viscoelasticity on cellular behaviour. Nature 2020;584:535–46 [PubMed: 32848221]
17. Charrier EE, Pogoda K, Li R, Wells RG, Janmey PA. Elasticity-dependent response of malignant cells to viscous dissipation. Biomech Model Mechanobiol 2020
18. Tilghman RW, Cowan CR, Mih JD, Koryakina Y, Gioeli D, Slack-Davis JK, et al. Matrix rigidity regulates cancer cell growth and cellular phenotype. PloS one 2010;5:e12905 [PubMed: 20886123]
19. Seager RJ, Hajal C, Spill F, Kamm RD, Zaman MH. Dynamic interplay between tumour, stroma and immune system can drive or prevent tumour progression. Convergent Science Physical Oncology 2017;3:034002 [PubMed: 30079253]
20. Maller O, Drain AP, Barrett AS, Borgquist S, Ruffell B, Thanh PT, et al. Inflammation promotes tumor aggression by stimulating stromal cell-dependent collagen crosslinking and stromal stiffening. bioRxiv 2020:2020.02.13.948141
21. Park SY, Kim HM, Koo JS. Differential expression of cancer-associated fibroblast-related proteins according to molecular subtype and stromal histology in breast cancer. Breast cancer research and treatment 2015;149:727–41 [PubMed: 25667103]
22. Butcher DT, Alliston T, Weaver VM. A tense situation: forcing tumour progression. Nat Rev Cancer 2009;9:108–22 [PubMed: 19165226]
23. Conklin MW, Eickhoff JC, Riching KM, Pehlke CA, Eliceiri KW, Provenzano PP, et al. Aligned collagen is a prognostic signature for survival in human breast carcinoma. The American journal of pathology 2011;178:1221–32 [PubMed: 21356373]
24. Mason TG, Weitz DA. Optical measurements of frequency-dependent linear viscoelasticity moduli of complex fluids. Phys Rev Lett 1995;74:1250–3 [PubMed: 10058972]
25. Hajjarian Z, Nadkarni SK. Evaluation and correction for optical scattering variations in laser speckle rheology of biological fluids. PloS one 2013;8:e65014 [PubMed: 23705028]
26. Hajjarian Z, Nadkarni SK. Correction of optical absorption and scattering variations in laser speckle rheology measurements. Optics express 2014;22:6349–61 [PubMed: 24663983]
27. Hajjarian Z, Nadkarni SK. Estimation of particle size variations for laser speckle rheology of materials. Opt Lett 2015;40:764–7 [PubMed: 25723427]
28. Hajjarian Z, Tripathi MM, Nadkarni SK. Optical Thromboelastography to evaluate whole blood coagulation. J Biophotonics 2015;8:372–81 [PubMed: 24700701]
29. Hajjarian Z, Nia HT, Ahn S, Grodzinsky AJ, Jain RK, Nadkarni SK. Laser Speckle Rheology for evaluating the viscoelastic properties of hydrogel scaffolds. Sci Rep 2016;6:37949 [PubMed: 27905494]
30. Hajjarian Z, Toussaint JD, Guerrero JL, Nadkarni SK. In-vivo mechanical characterization of coronary atherosclerotic plaques in living swine using intravascular laser speckle imaging. Biomedical optics express 2021;12:2064–78 [PubMed: 33996217]
31. Mason TG, Ganesan K, van Zanten JH, Wirtz D, Kuo SC. Particle Tracking Microrheology of Complex Fluids. Physical Review Letters 1997;79:3282–5
32. Dasgupta BR, Weitz DA. Microrheology of cross-linked polyacrylamide networks. Physical review E, Statistical, nonlinear, and soft matter physics 2005;71:021504

33. Mak M, Anderson S, McDonough MC, Spill F, Kim JE, Boussommier-Calleja A, et al. Integrated Analysis of Intracellular Dynamics of MenaINV Cancer Cells in a 3D Matrix. Biophysical journal 2017;112:1874–84 [PubMed: 28494958]
34. Luck AA, Evans AJ, James JJ, Rakha EA, Paish EC, Green AR, et al. Breast carcinoma with basal phenotype: mammographic findings. AJR American journal of roentgenology 2008;191:346–51 [PubMed: 18647900]
35. Joaquin D, Grigola M, Kwon G, Blasius C, Han Y, Perlitz D, et al. Cell migration and organization in three-dimensional in vitro culture driven by stiffness gradient. Biotechnology and bioengineering 2016;113:2496–506 [PubMed: 27183296]
36. Acerbi I, Cassereau L, Dean I, Shi Q, Au A, Park C, et al. Human breast cancer invasion and aggression correlates with ECM stiffening and immune cell infiltration. Integr Biol (Camb) 2015
37. Chikarmane SA, Tirumani SH, Howard SA, Jagannathan JP, DiPiro PJ. Metastatic patterns of breast cancer subtypes: what radiologists should know in the era of personalized cancer medicine. Clin Radiol 2015;70:1–10 [PubMed: 25300558]
38. Balleyguier C, Ciolovan L, Ammari S, Canale S, Sethom S, Al Rouhbane R, et al. Breast elastography: the technical process and its applications. Diagn Interv Imaging 2013;94:503–13 [PubMed: 23619293]
39. Evans A, Rauchhaus P, Whelehan P, Thomson K, Purdie CA, Jordan LB, et al. Does shear wave ultrasound independently predict axillary lymph node metastasis in women with invasive breast cancer? Breast cancer research and treatment 2014;143:153–7 [PubMed: 24305976]
40. Denis M, Gregory A, Bayat M, Fazzio RT, Whaley DH, Ghosh K, et al. Correlating Tumor Stiffness with Immunohistochemical Subtypes of Breast Cancers: Prognostic Value of Comb-Push Ultrasound Shear Elastography for Differentiating Luminal Subtypes. PloS one 2016;11:e0165003 [PubMed: 27776153]
41. McKnight AL, Kugel JL, Rossman PJ, Manduca A, Hartmann LC, Ehman RL. MR elastography of breast cancer: preliminary results. AJR American journal of roentgenology 2002;178:1411–7 [PubMed: 12034608]
42. Sinkus R, Siegmann K, Xydeas T, Tanter M, Claussen C, Fink M. MR elastography of breast lesions: understanding the solid/liquid duality can improve the specificity of contrast-enhanced MR mammography. Magn Reson Med 2007;58:1135–44 [PubMed: 17969009]
43. Plodinec M, Loparic M, Monnier CA, Obermann EC, Zanetti-Dallenbach R, Oertle P, et al. The nanomechanical signature of breast cancer. Nature nanotechnology 2012;7:757–65
44. Kennedy BF, McLaughlin RA, Kennedy KM, Chin L, Wijesinghe P, Curatolo A, et al. Investigation of Optical Coherence Microelastography as a Method to Visualize Cancers in Human Breast Tissue. Cancer Res 2015;75:3236–45 [PubMed: 26122840]
45. Kennedy KM, Zilkens R, Allen WM, Foo KY, Fang Q, Chin L, et al. Diagnostic Accuracy of Quantitative Micro-Elastography for Margin Assessment in Breast-Conserving Surgery. Cancer Res 2020;80:1773–83 [PubMed: 32295783]
46. Loh QL, Choong C. Three-dimensional scaffolds for tissue engineering applications: role of porosity and pore size. Tissue Eng Part B Rev 2013;19:485–502 [PubMed: 23672709]
47. Gardel MV, Weitz D. Microrheology. In: Breuer KS, editor. Microscale Diagnostic Techniques. Berlin, Heidelberg. : Springer; 2005.
48. Squires TM, Mason TG. Fluid Mechanics of Microrheology. Annual Review of Fluid Mechanics 2010;42:413–38
49. Ding J, Warren R, Girling A, Thompson D, Easton D. Mammographic density, estrogen receptor status and other breast cancer tumor characteristics. Breast J 2010; 16:279–89 [PubMed: 20408823]
50. Chamming's F, Latorre-Ossa H, Le Frere-Belda MA, Fitoussi V, Quibel T, Assayag F, et al. Shear wave elastography of tumour growth in a human breast cancer model with pathological correlation. Eur Radiol 2013;23:2079–86 [PubMed: 23553589]
51. Cohen IJ, Blasberg R. Impact of the Tumor Microenvironment on Tumor-Infiltrating Lymphocytes: Focus on Breast Cancer. Breast Cancer (Auckl) 2017;11:1178223417731565 [PubMed: 28979132]

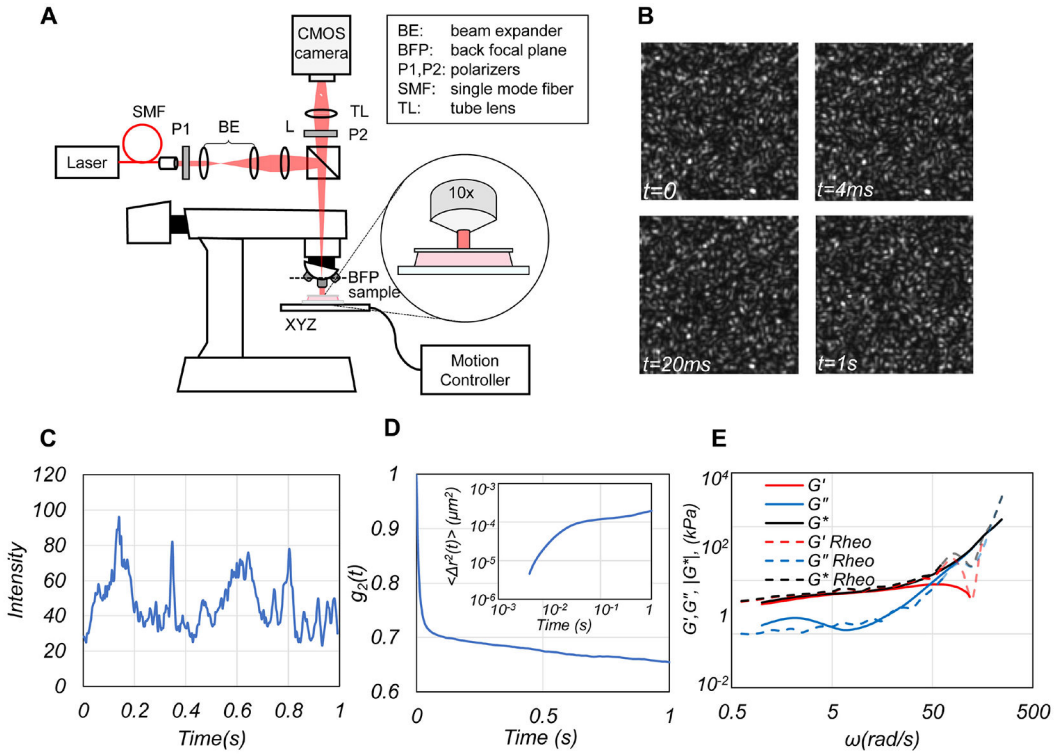

Figure 1. SHEAR platform.

(A) Schematic of the SHEAR optical set up. (B) Representative speckle frames acquired at 4 time points. (C) A representative trace of temporal speckle intensity fluctuations from a normal adipose breast tissue. (D) Cross-correlation of speckle fluctuations provides the speckle intensity autocorrelation, $g_2(t)$, from which the mean square displacement (MSD) of particles is deduced (inset). (E) Substituting the MSD in the GSER returns $|G^*(\omega)|$, $G'(\omega)$ and $G''(\omega)$ (Supplementary Method 1).

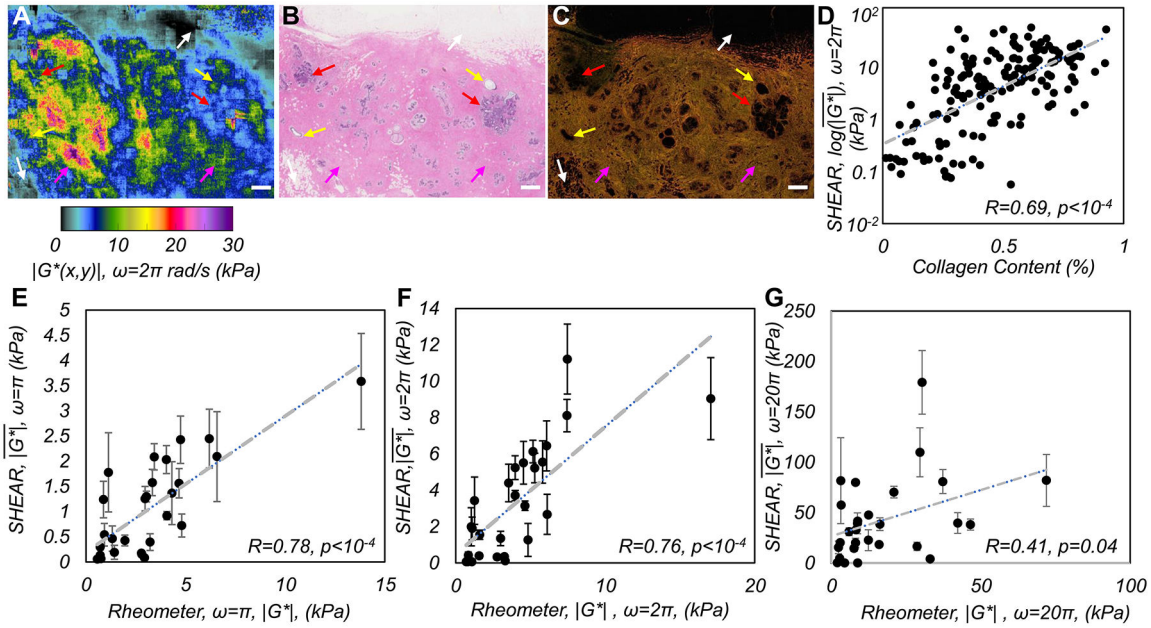

Figure 2. SHEAR validation.

(A) |G*(x,y,ω)| map of a normal human breast tissue evaluated at ω=2πrad/s (f=1Hz). (B) The corresponding H&E and (C) PSR sections. Scale bars: 1 mm. (D) $\overline{|G^*|}$ shows a strong positive correlation with total collagen measured from PSR sections (r=0.69, $p<10^{-4}$). (E-G) Scatter diagrams of $\overline{|G^*|}$, measured by SHEAR and conventional rheometry showing a strong, significant correlation at ω: π and 2π, which is lower at 20π rad/s (f:0.5, 1, and 10 Hz).

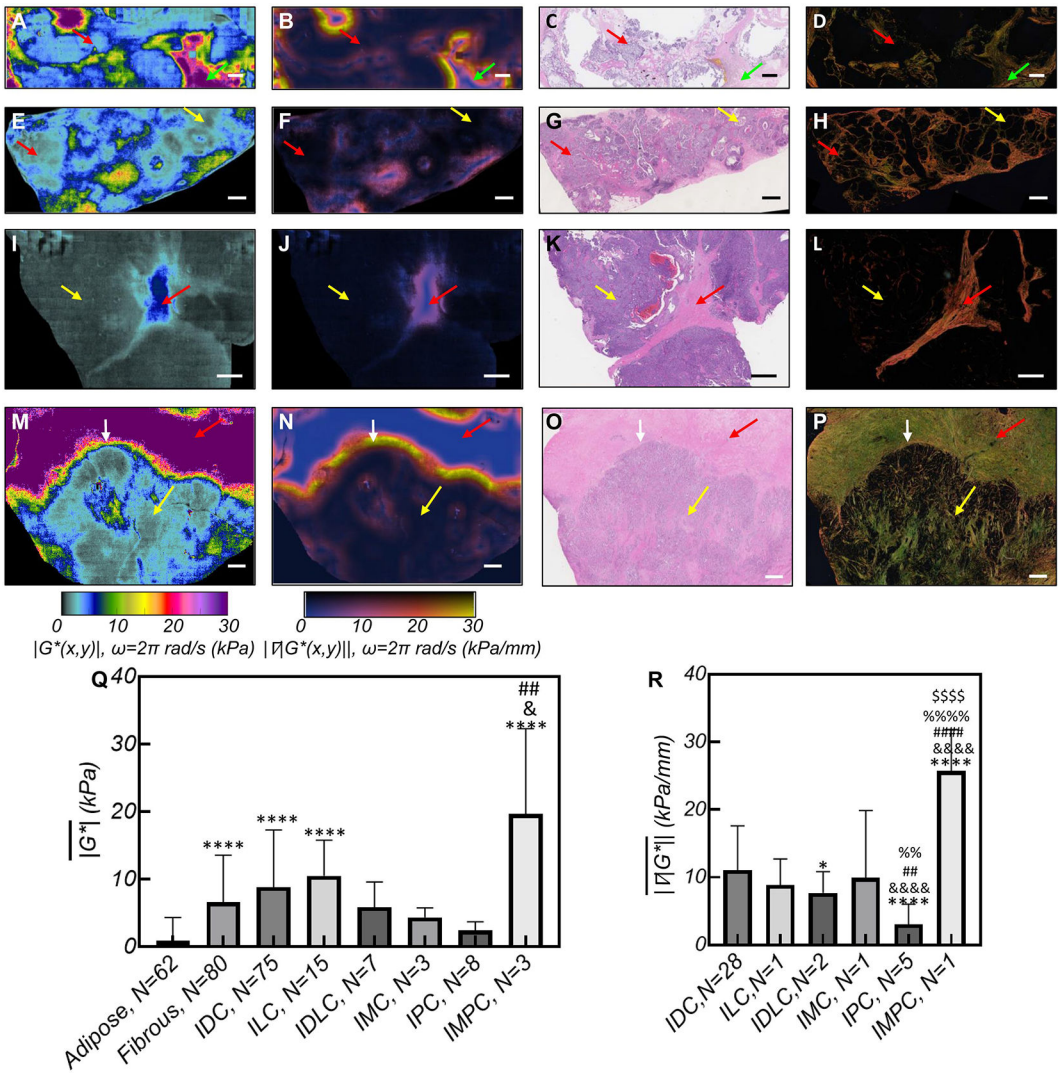

Figure 3. SHEAR |G*(x,y)| maps of histopathological subtypes.

(A) |G*(x,y)| maps of an invasive mucinous carcinoma (IMC). In softer mucinous regions (red arrow) |G*(x,y)| ~0.2-3 kPa, whereas in the stiffer fibrous ECM (green arrow) |G*(x,y)| ~ 30 kPa. (B) The corresponding |∇|G*(x,y)|| is elevated at the epithelium-stroma interface. (C) H&E slide shows tumor cells floating within mucin. (D) PSR section reveals the mucin-collagenous ECM interface. (E) |G*(x,y)| maps of an invasive ductal carcinoma (IDC) with a ductal carcinoma in situ (DCIS) component. In the epithelium, |G*(x,y)| ~ 1-5 kPa (yellow arrow), which increases in the ECM to ~ 20 kPa (red arrow); (F) The corresponding |∇|G*(x,y)||; (G) H&E, and (H) PSR. (I) |G*(x,y)| map of an invasive papillary carcinoma (IPC), showing |G*(x,y)| ~0.1-5 kPa in papillary cores (yellow arrow), and stalk (red arrow); (J) The corresponding|∇|G*(x,y)||; (K) H&E, and (L) PSR. The H&E presents the papillary histopathology and the PSR highlights the fibrous stalk. (M) |G*(x,y)| map of an invasive micro-papillary carcinoma (IMPC) shows that in the epithelium |G*(x,y)| ~3 kPa (yellow arrow) and that |G*(x,y)| is elevated in the ECM to ~ 30 kPa (red arrows); (N) The corresponding |∇|G*(x,y)||; (O) H&E, and (P) PSR. Scale bars: 1 mm. (Q) Bar

plots of the $\overline{|G^*|}$ for breast tissue of various histopathological diagnosis. Error bars are standard deviation. Symbols indicate the significance level when compared to adipose:*, fibrous:&, IPC:# (R) Bar plots of the $\overline{|\nabla|G^*||}$. Symbols indicate the significance level when compared to IDC:*, ILC:&, IDLC:#:, IMC:%, IPC:$. All |G*(x,y)| and |∇|G*(x,y)|| maps and bar plots are computed at $\omega=2\pi$ rad/s (f=1Hz).

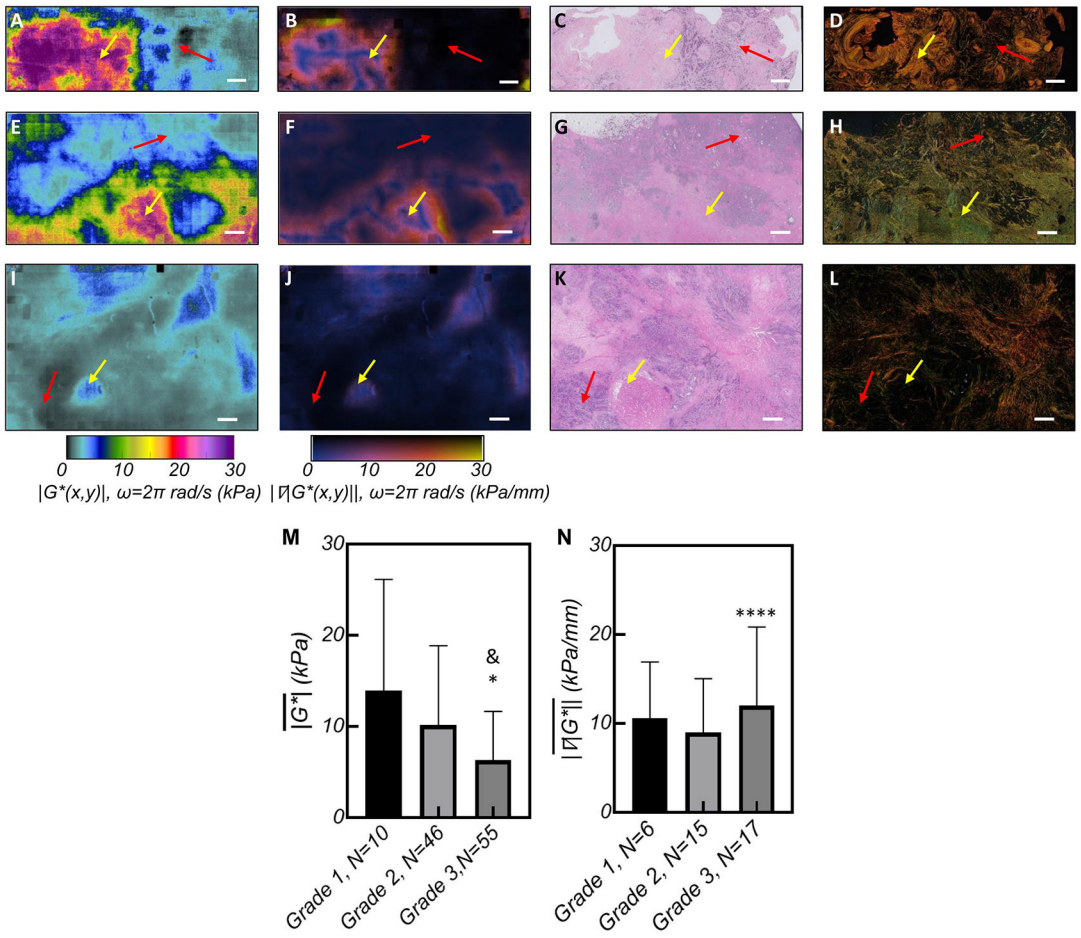

Figure 4. SHEAR |G*(x,y)| maps of histological grades.

(A) |G*(x,y)| and (B) |∇|G*(x,y)‖ maps of a grade 1 IDC, (C) The H&E section shows the tumor epithelium and ECM coincide with complaint (~0.1-8kPa, red arrow) and stiffer areas (~10-30kPa, yellow arrow) in the |G*(x,y)| map with elevated |∇|G*(x,y)‖ at the interface. (D) PSR shows dense collagen at sites of increased |G*(x,y)|. (E) |G*(x,y)| and (F) |∇|G*(x,y)‖ maps of a grade 2 invasive lobular carcinoma (ILC). (G) The H&E shows the tumor epithelium at the top corresponding with lower |G*(x,y)|~ 0.1-4 kPa (red arrow) and the stiffer ECM at the bottom (yellow arrows). (H) PSR reveals dense collagen at areas of increased |G*(x,y)|. (I) |G*(x,y)| map of a Grade 3 IDC; with patches of |G*(x,y)|~2 kPa, interspersed with regions of |G*(x,y)| ~ 5 kPa; (J) The corresponding |∇|G*(x,y)‖ shows the faint contrast between these regions; (K) H&E depicts aggressive tumor cells (red arrow) at the sites of extremely reduced |G*(x,y)| near the necrotic core (yellow arrow); (L) Low level collagen staining in the corresponding PSR image. Scale bars: 1 mm. (M) Bar plots of the $\overline{|G^*|}$ and (N) $\overline{|\nabla|G^*||}$ for tumors of different histopathological diagnosis. Error bars depict standard deviation and the symbols indicate the significance level when compared to grade 1:* and grade 2:&. All |G*(x,y)| and |∇|G*(x,y)‖ maps and bar plots are computed at ω=2π rad/s (f=1Hz).

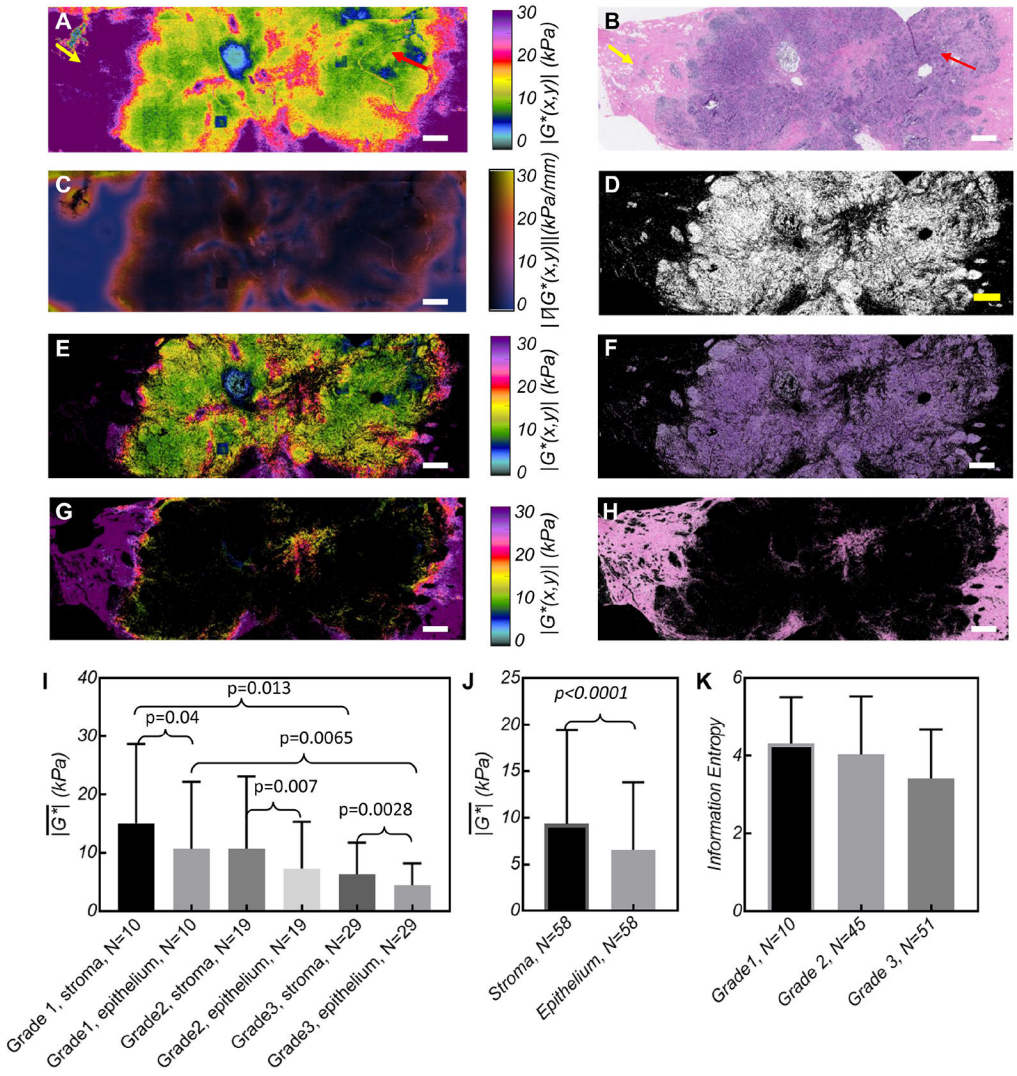

Figure 5. SHEAR assessment of mechanical heterogeneity.

(A) |G*(x,y)| maps of a grade 1 IDC, with a central area of |G*(x,y)|~0.5-10 kPa (red arrow), and periphery of |G*(x,y)| ~10-30 kPa (yellow arrow) (B) H&E slide shows the corresponding cellular epithelial and stroma regions. (C) The ‖∇|G*(x,y)|‖ is elevated at the epithelium-stroma interface. (D) The epithelium mask derived from the color space analysis of the H&E section (see Supplementary Method 4). (E, G) Spatially resolved separation of |G*(x,y)| maps within the tumor epithelium and stroma. (F, H) The pixels of the H&E image corresponding to the epithelial and stromal clusters. (Scale bar: 1 mm). (I) Bar plots displaying the $\overline{|G^*|}$ within the tumor stroma and epithelium, across different grades (for 58 tumors with a distinct epithelial-stroma components). Paired t-tests show significant elevation of $\overline{|G^*|}$ in the stromal vs the epithelial components within each grade. In addition, un-paired t-test indicate that the $\overline{|G^*|}$ of the stroma and epithelium are significantly different between grades 1 and 3. (J) Bar diagram of $\overline{|G^*|}$ within stroma and epithelium of the tumor, grouped regardless of tumor grade. Paired t-test showed increased $\overline{|G^*|}$ in the stroma compared with the epithelium, regardless of grade ($p<0.0001$). (K)

Bar diagram of the information entropy of $|G^*(x,y)|$ maps across all tumors of various grades. Although the data shows a trend towards lower entropy at higher grades ($p<0.04$), Tukey analysis of multiple comparisons between grades is not significant. All $|G^*(x,y)|$ and $\|\nabla|G^*(x,y)|\|$ maps and bar plots are computed at $\omega=2\pi$ rad/s (f=1Hz).

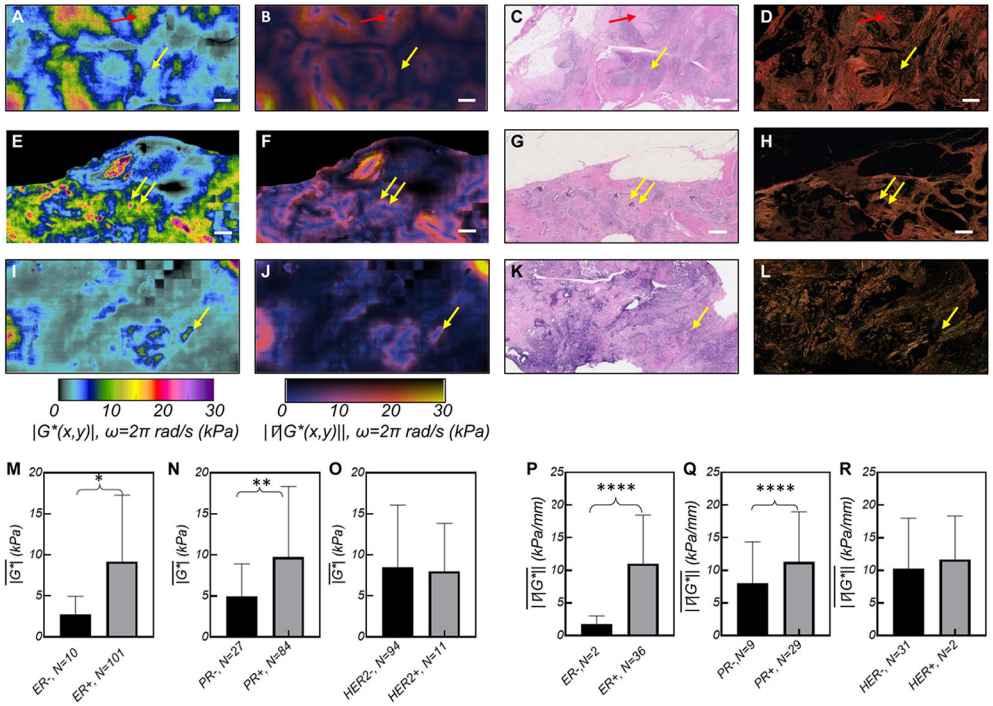

Figure 6. SHEAR |G*(x,y)| maps of breast tumors with different molecular receptors.

(A) |G*(x,y)| map of a Grade 3, ER/PR+, HER2−, ILC. The corresponding (B) |∇|G*(x,y)‖; (C) H&E, and (D) PSR sections. The H&E image reveals adipocytes, tumor cells, and degenerated collagen fibers in softer regions of ~5 kPa (yellow arrow) and pauci-cellular fibrous ECM in stiffer areas of ~10kPa (red arrow). (E) |G*(x,y)| map of a Grade 3, ER/PR/HER2+ IDC tumor with DCIS components. The map has a background of |G*(x,y)|< 5kPa, islands of |G*(x,y)| < 10 kPa, and sporadic spots of |G*(x,y)|> 30 kPa (yellow arrows); (F) The corresponding |∇|G*(x,y)‖ shows excellent sensitivity in detecting the stromal interface. (G) The H&E image reveals necrotic calcifications at stiff spots (yellow arrows) that are not visible in (H) the PSR image. (I) |G*(x,y)| map of a Grade 3, IDC, ER/PR/HER2− showing mostly compliant area of <5 kPa, with occasional islands of increased |G*(x,y)| ~ 5 – 10 (J) |∇|G*(x,y)‖ shows an overall low gradient. (K) H&E image presents high grade tumor cells, inflammatory lymphocytes and histiocytes, and necrosis. (L) The PSR image features collagen fibrils laced around tumor cells. (Scale bars: 1 mm). Bar diagrams, comparing $\overline{|G^*|}$ in tumors with: (M) ER− and ER+; (N). PR− and PR+; (O) HER2− and HER2+. Bar diagrams comparing $\overline{|\nabla|G^*||}$ in tumors with: (P) ER− and ER+; (Q). PR− and PR+; (R) HER2− and HER2+. The stars indicate the significance level of the un-paired t-test, used to compare the groups. ($p<0.05$: *,$p<0.01$: **,$p<0.001$: ***,$p<0.0001$: ****). All |G*(x,y)| and |∇|G*(x,y)‖ maps and bar plots are computed at $\omega=2\pi$ rad/s (f=1Hz).

Table 1.

Tumor Diagnoses and average shear moduli.

Diagnosis/Type	Number	$\overline{\lvert G^* \rvert}$ (kPa)
Histological type		
Invasive Ductal Carcinoma (IDC)	75	8.8±8.5
Invasive Lobular Carcinoma (ILC)	15	10.5±5.3
Invasive Ductal-Lobular Carcinoma (IDLC)	7	5.9±3.7
Invasive Mucinous Carcinoma (IMC)	3	4.4±1.4
Invasive Papillary Carcinoma (IPC)	8	2.4±1.3
Invasive Micropapillary Carcinoma (IMPC)	3	19.7±12.6
Histological grade		
Grade 1	10	13.9±12.2
Grade 2	46	10.2±8.7
Grade 3	55	6.3±5.3
Estrogen Receptor (ER) status		
ER+	101	9.2±8.1
ER−	10	2.8±2.2
Progesterone Receptor (PR) status		
PR+	84	9.7±8.6
PR−	27	5±3.9
Human epidermal Growth Factor Receptor 2 (HER2) status		
HER2+	11	8±5.8
HER2−	94	8.5±7.6
HER2-equivocal	6	11.7±15.5
Lymph node (LN) status		
Positive	54	9.1±7.1
Negative	49	9.2±9.15
Unknown	8	3.2±1.7
Total	111 carcinomas (out of 251 samples)	